

SUPPLEMENTAL MATERIAL

1. *Cosmogenic Nuclides: Sampling strategy, treatment, and calculation*

Secondary cosmic rays make cosmogenic radionuclides when they meet oxygen in the atmosphere or rocks. In rocks, radionuclides beryllium-10 is made in a silicate mineral, e.g., Quartz. This method can help us understand timing and the rate of landscapes evolution by measuring the concentrations (Lal, 1991).

We measured *in situ* exposure ages using ^{10}Be for three sites. Twelve bedrock samples were collected on each surface of bedrock strath terraces of main trunk streams draining the Ste. Francois Mountains (Castor River Shut-in, Millstream Garden Shut-in on the St. Francois River) and one tributary stream (Stout Creek on the St. Francois). Two samples (Ozark 13, 14) were taken from a ridgetop drainage divide. We measured the elevation of each sampling site with dGPS to obtain cm-precision elevations and used the age-elevation date to calculate incision rate for each strath terrace flight (Fig. S1).

We also measured millennial catchment-wide erosion rates using ^{10}Be isotopes from five drainage basins (Castor River, St. Francois River, Black River, Big River, and Pickle Creek) (Fig. S2). We collected sand samples at basin outlets to measure the denudation rates of the whole catchments. We also collected samples to measure the denudation rates of sub-catchment nested in the Mesoproterozoic granites and rhyolites and Paleozoic sedimentary rocks. In an attempt to assess whether human impact (agriculture, civilization) causes higher denudation rate, samples in St. Francois River were collected along the main stem, and one of the samples in Pickle Creek was taken on a farm field near a channel.

Chemical procedures for ^{10}Be concentrations were performed at the Korea University, Seoul, South Korea. Organic and carbonate materials were removed in $\text{HCl-H}_2\text{O}_2$. HF-HNO_3 leaching (3–1% depending on purity) in the ultra-sonicator for 12 hours. Magnetic separation removed mafic minerals using a magnetic separator and by handpicking. After dissolution with a low-background ^9Be carrier ($2 \times 10^{-15} \text{ }^{10}\text{Be}/^9\text{Be}$), fluorides were fumed out using HClO_4 and HNO_3 . The Be ion was separated by ion exchange and precipitated at a $\text{pH} > 7$ (Kohl and Nishiizumi, 1992). Be hydroxides were dried and oxidized at 800°C for 10 min in a furnace. Finally, BeO was mixed with niobium (Nb) and loaded into targets.

The BeO targets were measured using accelerator mass spectrometry (AMS) at the Korea Institute of Science and Technology (KIST), Seoul, Korea. Measured $^{10}\text{Be}/^9\text{Be}$ ratios were corrected using a blank and standards prepared by Nishiizumi et al. (2007) for a ^{10}Be half-life of $(1.387 \pm 0.03) \times 10^6 \text{ yr}$ (Chmeleff et al., 2010; Korschinek et al., 2010).

We applied the CAIRN model to convert the ^{10}Be concentration to catchment-wide denudation rates (Mudd et al., 2016). The CAIRN method calculates the catchment-averaged production rate and a shielding factor pixel-by-pixel in the catchment. We used DEMs with 10 m resolution. The model is supported the four exponential approximations of Braucher et al. (2009) to predict cosmogenic radionuclide production from spallation and muons. We used the time-independent air pressure scaling schemes (Lal, 1991; Stone,

2000) to convert elevation and latitude to air pressure (Balco et al., 2008). We also used a uniform density of 2650 kg/m^3 and a ^{10}Be production rate of $4.30 \pm 0.31 \text{ g}^{-1} \text{ yr}^{-1}$ for sea level at high latitudes (Stone, 2000; Balco et al., 2008).

Exposure ages from three *in situ* strath terrace sites measured in this study vary from $13 \pm 1 \text{ mm/ka}$ to $175 \pm 16 \text{ mm/ka}$. As discussed above, we combined these ages with dGPS-determined elevations to calculate incision rates for the three sites. Each site showed a clear linear fit to the age-elevation data.

Catchment-wide erosion rates from 11 drainage basins measured in this study vary from $5.7 \pm 1.3 \text{ mm/ka}$ to $14.2 \pm 3.3 \text{ mm/ka}$. The highest erosion rates were obtained from Big River ($13.5 \pm 3.2 \text{ mm/ka}$) and Pickle Creek ($14.2 \pm 3.3 \text{ mm/ka}$). The lowest erosion rate was obtained from Clark Creek, $5.7 \pm 1.3 \text{ mm/ka}$, a tributary of the St. Francois River. We exclude the denudation rates from Pickle Creek and Big River because sampling location (farm field) might have given a high denudation rate because of human impact (agriculture).

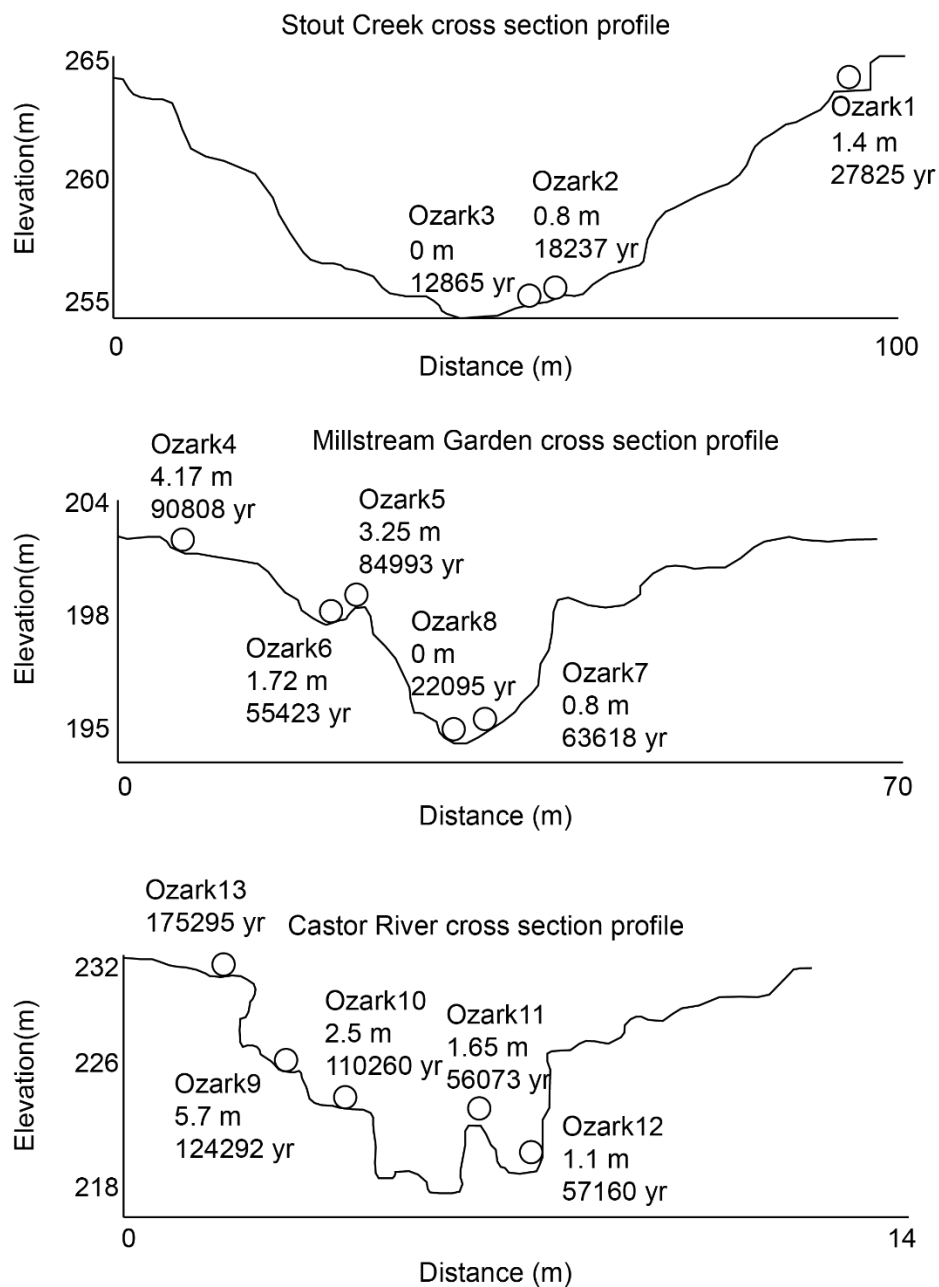


Figure S1. Cross section view of three bedrock strath terraces systems. Stout Creek is a tributary of the St. Francois River. Millstream Garden is located on the main trunk of the St. Francois River. The Castor River shut-in profile is located on the main trunk of the Castor River.

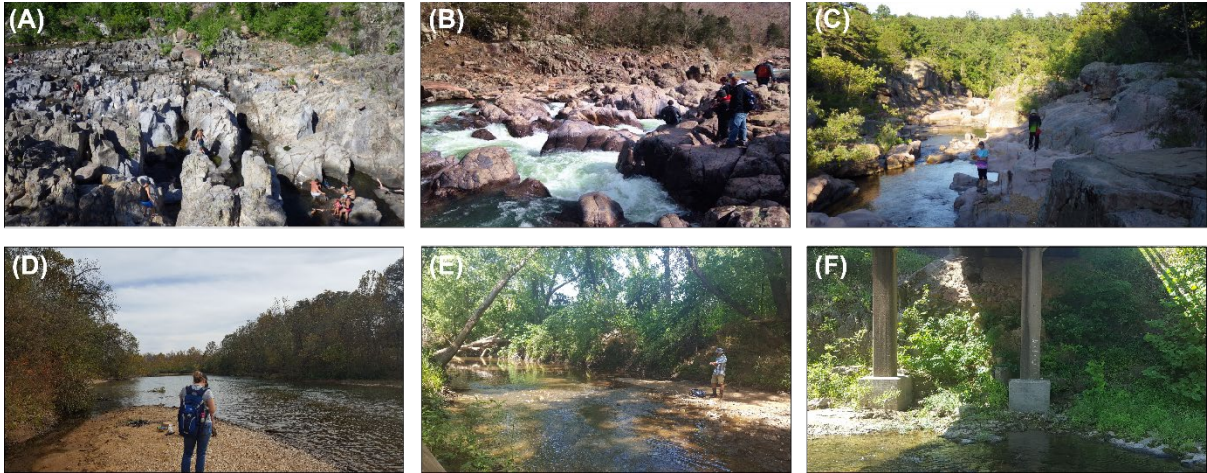


Figure S2. Sampling photos. We collected *in situ* bedrock samples for incision rates on the strath terraces, and sand samples for CWDRs on active sand bars at: (A): Johnson shut-in, (B): Millstream Garden shut-in, (C) Castor River shut-in, and (D), (E) and (F) show CWDR sand sample photos that we visited during the dry period (July) when we sampled active sand bars.

2. Schmidt Hammer Rebound Measurements

We measured Schmidt hammer rebound values (Fig. S3). Measurements were conducted following standard procedures (e.g., Aydin and Basu, 2005), and at least 125 impacts per measurement were made on dry exposures of primary lithologies exposed on bedrock strath terraces. Outcrops measured were both dated and undated terraces surfaces. Measurement points were distributed across the bedrock outcrops and made away from joints and cracks to obtain representative measurements that capture the variability on any single strath surface.

To avoid anomalous reduced R values procedures we followed outlined by Viles et al. (2011). The Schmidt hammer was used perpendicular to the surface, avoiding rough, irregular and lichen-covered surfaces. Additionally, we worked to avoid other contentious issues, particularly regarding operator variance. In this study, three of the authors (DEK, YBS, JCW) sampled all surfaces, and therefore, procedures and results should be internally consistent. R values were collected for the following lithology: rhyolite and granite. Measuring done on calibration sites where two or more surfaces had been dated, which ensured that anomalous results could be more easily identified.

All three sites (Johnson Shut-in, Castor Shut-in, and Stout Creek Shut-in) are on rhyolite and granite. We calculated and present the averages and two standard deviations of all measurements and give rock types from each calibration location below (from highest to lowest strath terraces), in Table S1, and show our calibration regression fit in Fig. S4. The Johnson Shut-in site terraces have R values of 64.11 ± 3 , 64.14 ± 4 , and 69.64 ± 3 . The Castor shut-in site terraces have R values of 60.52 ± 4 , 60.25 ± 3 , 63.2 ± 3 and 59.92 ± 3 . The Stout Creek shut-in terraces have R values of 64.28 ± 3 , 68.31 ± 3 , and 69.22 ± 3 .

The results of Schmidt hammer R-values indicate that the mean values measured near the channel are higher than those from higher terrace surfaces. Since we have not calibrated our R-values with the compressive or tensile rock strength measurements in the laboratory (e.g., Murphy et al., 2016), our measured R-values should be considered to represent the relative strengths of rocks at these sites.



Figure S3. Castor shut-in on the Castor River.

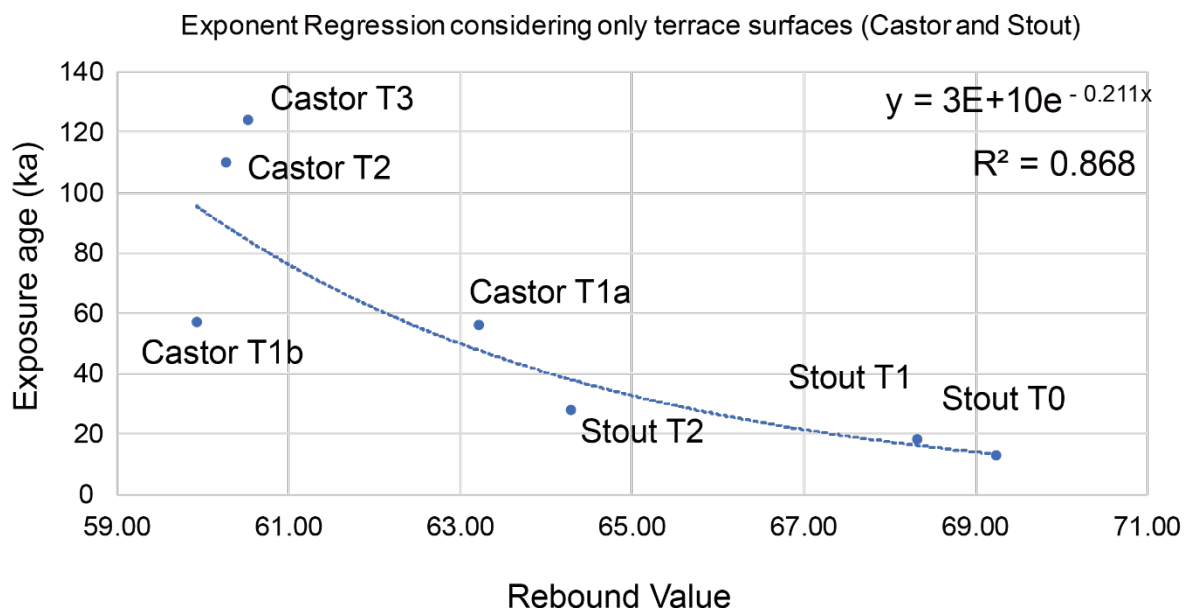


Figure S4. Exponent regression fit derived for Schmidt hammer R measurements and age.

Table S1. Result of rebound (R) values measured by Schmidt hammer.

Measurement site	Site	Mean rebound value	Standard deviation	¹⁰ Be exposure ages (yr)	Exposure ages from SH (yr)
Castor	T3	60.52	3.52	124,292	
	T2	60.26	3.13	110,260	
	T1a	63.20	2.51	56,072	
	T1b	59.92	2.88	57,160	
	T0	68.32	3.69		16,464
Stout Creek	T2	64.28	3.12	27,825	
	T1	68.31	3.32	18,237	
	T0	69.22	2.77	12,865	
Johnson Shut-in	US1	64.15	4.14		41,137
	US2	69.64	2.89		12,462
	LS1	64.11	3.69		40,008

3. Quantification of Topographic Parameters

We calculated topographic metrics, including slope, local relief, and channel steepness, for each basin using ArcGIS and TopoToolbox in Matlab (Schwanghart and Scherler, 2014) (Table S3). We used the 10 m DEM from USGS (<https://earthexplorer.usgs.gov/>). The slope is calculated along the steepest descent direction in an 8-cell neighborhood, and local relief is calculated as the elevation difference between the highest and lowest elevations within a 1 km radius circular window. For channel steepness (k_{sn}), we extracted channel points with drainage areas larger than 1 km² and calculated basin-averaged k_{sn} through two methods; by (1) the integral method based on χ (Perron & Royden, 2013; Scherler et al., 2017) and (2) averages of channel steepness that are calculated as normalized channel slope by drainage area (Wobus et al., 2006; Ouimet et al., 2009; Kirby and Ouimet, 2011; Scherler et al., 2017). In the integral method, channel steepness k_s [L^{2θ}] is calculated from the fit between elevation z and χ (Perron and Royden, 2013). We calculated normalized channel steepness (k_{sn}) assuming a reference concavity θ of 0.45, which is consistent with previous studies of this area (Beeson et al., 2017), plotting the longitudinal profiles with log slope-log area respectively (Fig S5, S6, and S7) and chi-elevation profiles (S8).

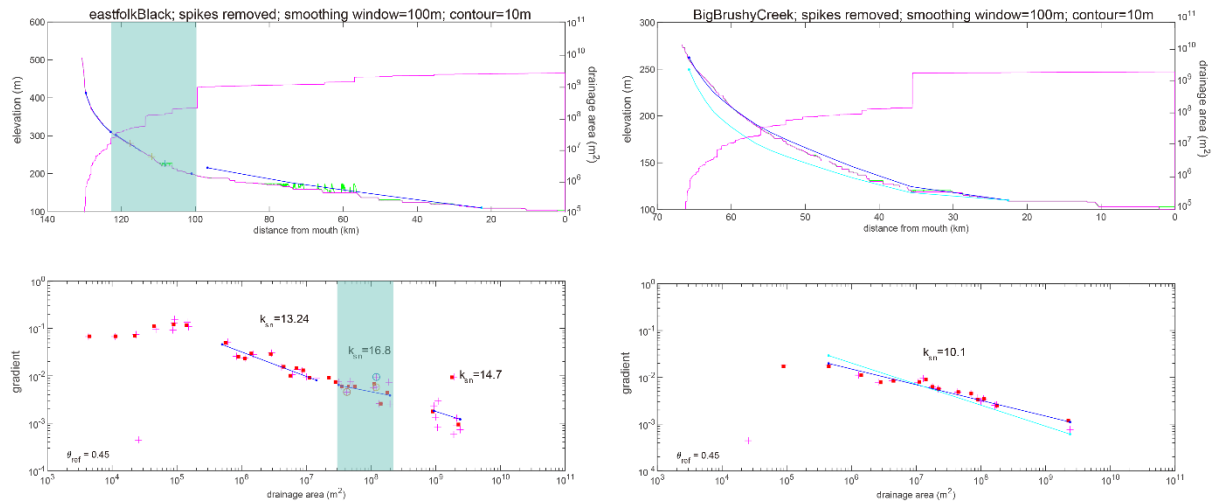


Figure S5. Channel profile and log slope-log area plot on Black River. Left: East Folk Black River across the Proterozoic rhyolite and granite. Right: Big Brushy Creek across the Paleozoic sedimentary rock only.

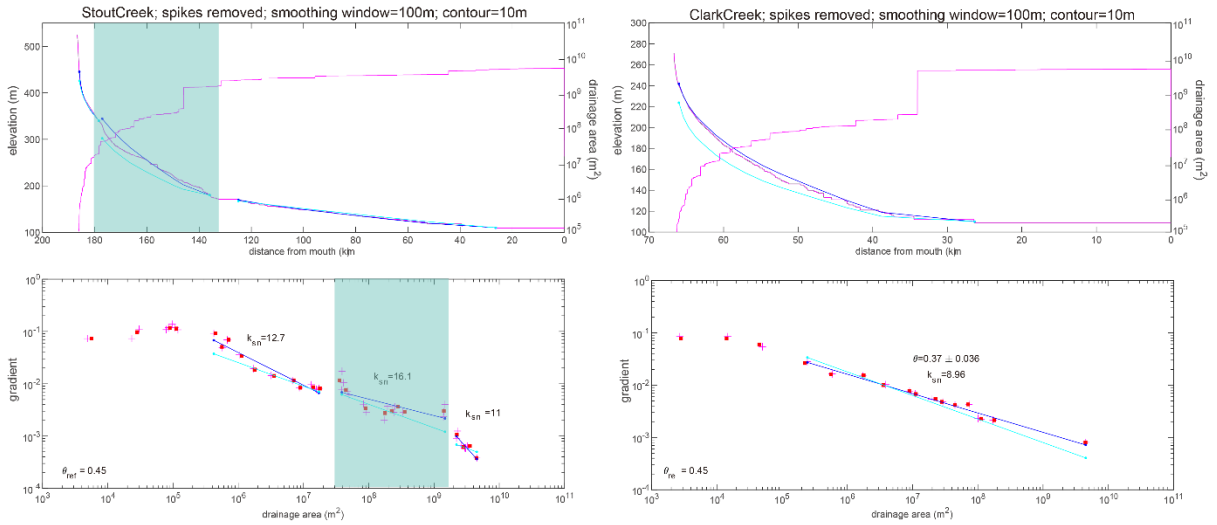


Figure S6. Channel profile and log slope-log area plot on St. Francois River. Left: Stout Creek, a tributary of St. Francois River, across the Mesoproterozoic igneous rock. Right: Clark Creek across the Paleozoic sedimentary rock.

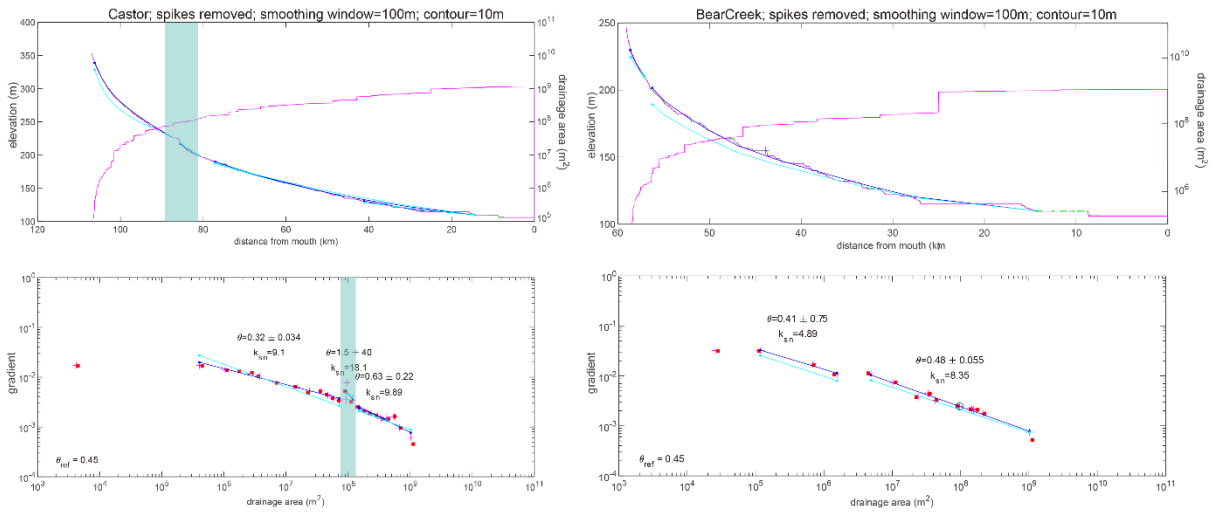


Figure S7. Channel profile and log slope-log area plot on Castor River. Left: Castor River, main stem, across the Mesoproterozoic sedimentary rock. Right: Bear Creek across Paleozoic sedimentary rock only.

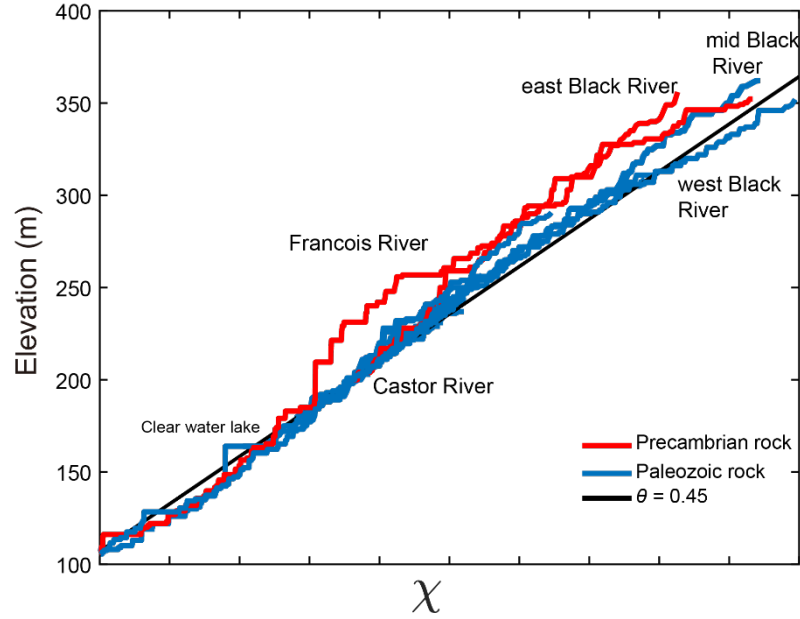


Figure S8. Chi-elevation graph. Two channels (St. Francois River and east Black River) across the Proterozoic sedimentary rock show significant knickpoints (red lines), whereas the slopes of other channels are across Paleozoic sedimentary rocks and corresponding with steady state conditions (black line).

Basin-averaged slopes range from $3.37 (\pm 2.7)$ to $11.7 (\pm 6.9)$ degree, and basin-averaged local relief range from $44 (\pm 14)$ to $141 (\pm 39)$ m. Basin-averaged channel steepness, k_{sn} , range from $6.4 (\pm 3.2)$ to $16.4 (\pm 7.2) \text{ m}^{0.9}$ (Table S3; Fig. 2). We quantified lithology for each basin based on a lithological map by MEGA2007. We defined two rock classifications Paleozoic sedimentary rocks (Cambrian, Ordovician) and Proterozoic igneous rocks (d,l,v). Most basins consist of multiple lithologies. We focus on small basins dominated by the Paleozoic rock (far from St. Francois Mountain, and dominated by Proterozoic igneous rock in the St. Francois Mountains (Fig. S9). Note that morphologic parameters on the Mesoproterozoic igneous rock are for the most part systematically higher than those same parameters on the Paleozoic sedimentary rocks.

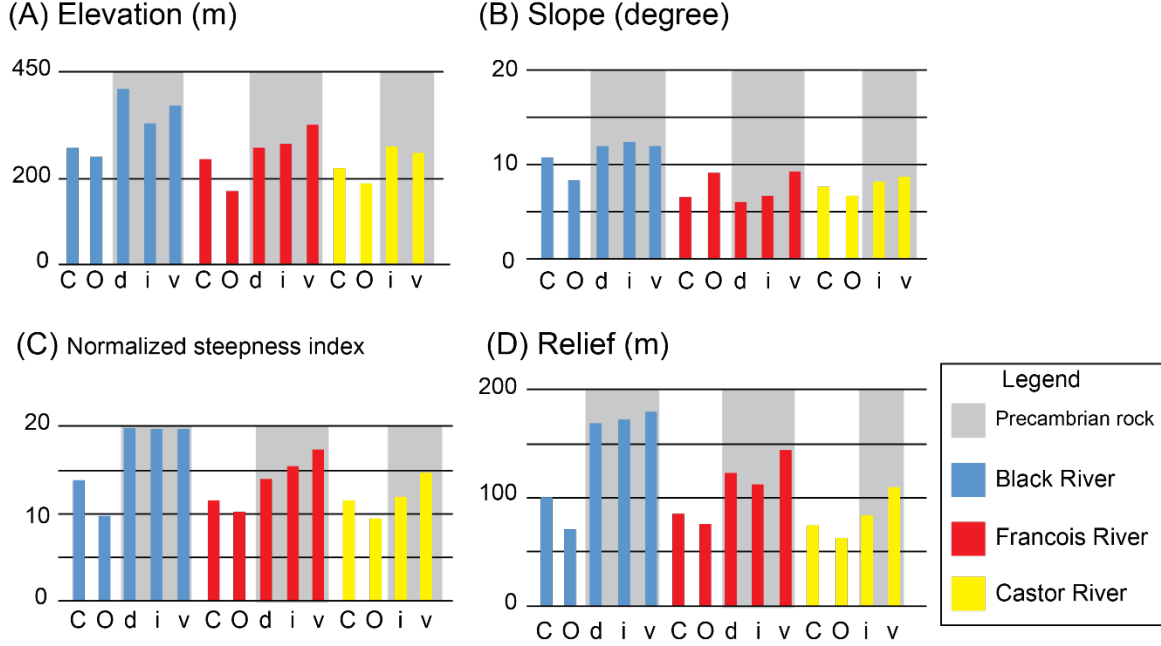


Figure S9. Histogram of morphologic indices showing strong dependency on lithology.

4. Formal bedrock erodibility calculations

CRN-derived denudation rates and normalized channel steepness data were used to calibrate erosion in the incision model by constraining the bedrock erodibility of St. Francois Mountain. Upstream area-based stream power model (Howard et al, 1994) is the first approach to represent river incision:

$$E = K \cdot A^m \cdot S^n \quad (1)$$

Where E is the long-term fluvial incision rate, K is the erodibility, A is the upstream area, S is the channel slope, and m and n are exponents. Equation (1) can be rewritten as:

$$E = K \cdot k_s^n \quad (2)$$

When we assumed normalized steepness index ($\theta (=m/n) = 0.45$, $m=0.45$, $n=1$), Equation (2) can be rewritten as:

$$K = E/k_{sn} \quad (3)$$

Under the assumption that K is constant along with the stream profile, a reasonable assumption for uniform lithology (Snyder et al., 2000), this relationship guides the calibration of stream power in Equation 3. To constrain K , we used the standard deviation of CRN-derived basin erosion rates for E and the mean k_{sn} in Equation 3. This attempt resulted in a range of K values for the Precambrian rock and the Paleozoic rock but did not

yield any important insights that enhance the strong lithologic dependency determined above (Fig. S9).

5. Calculating isostatic rebound using isostatic-flexural Flexure module in LandLab

To estimate the amount of erosion in the study area, we made the pre-incision surface from the present ridgelines by extracting points along divides from 30m size of Shuttle Radar Topography Mission (SRTM). We then interpolated and created a smoothed pre-incision surface with 1 km resolution which allowed us to calculate the eroded volume. We also used a topo to raster toolbox in ArcGIS. To avoid topographic inversion, we have added more points at bulging zones to guide the interpolate processes (Elez et al., 2020).

We also applied the bedrock erosion rate determined at the ridgetop (3mm/ka) at Elephant Rock State Park by Cremeens et al. (2005). To establish the change of topography over the various timescales, we used the 300ka exposure age from Elephant Rock, 800ka for glacier-inter glacier climate timescale, and 2.65 Ma for the entire Quaternary-Holocene. Once paleotopographic surfaces were obtained, the total eroded volumes was then calculated using ArcGIS (Fig S7).

We tested and calculate isostatic rebound with a two- dimensional elastic plate with point erosional unloading (e.g., Champagnac et al., 2007; Zhang et al., 2014). We varied the flexure component in the Landlab Flexure module (Hutton and Syvitski, 2008; Lambeck, 1988). To calculate the eroded volume, we subtracted the pre-incision surface from the current surface and converted it to pressure. We used various elastic thickness effects (20, 39, 50 and 170 km) taken from Bechtel et al. (1990), and McKenzie and Fairhead (1997). To model differences between the Paleozoic sedimentary rock and Proterozoic igneous rock, we assumed densities of $2,700 \text{ kg/m}^3$ for the Proterozoic igneous rock in the St. Francois Mountains and $2,400 \text{ kg/m}^3$ for the Paleozoic sedimentary rock around their flanks (Fig S10).

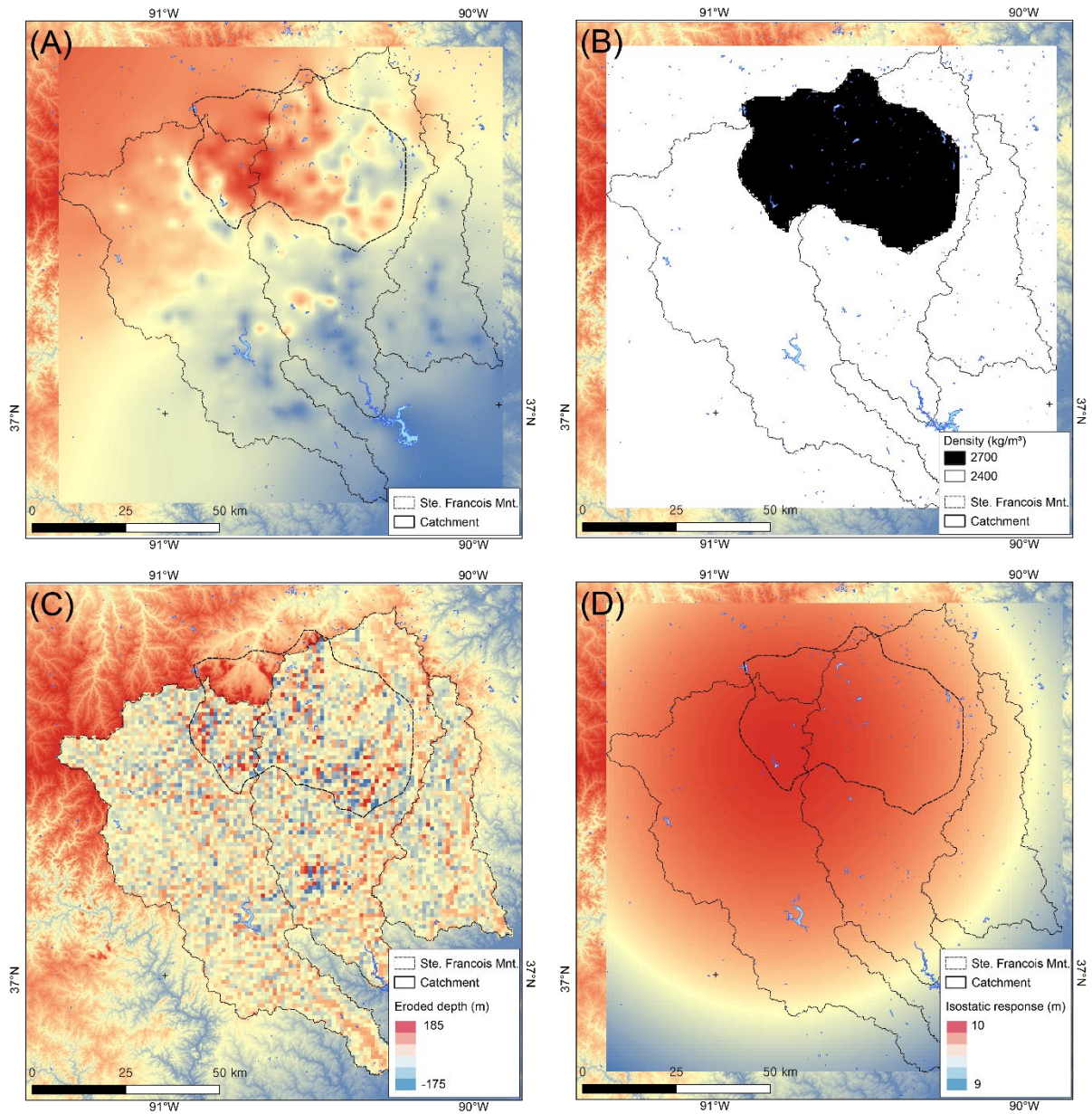


Figure S10. Establishment of isostatic-flexure model. (A): Interpolated present elevation of the late Quaternary paleo-surface (at ~300 ka). (B) Rock density map (1km size of resolution), surface area of Proterozoic igneous rocks shown in black. (C) Post-late Quaternary erosion obtained by subtracting present SRTM digital elevation model from interpolated paleo-surface. (D) Example isostatic-flexural uplift result ($T_e = 170$ km).

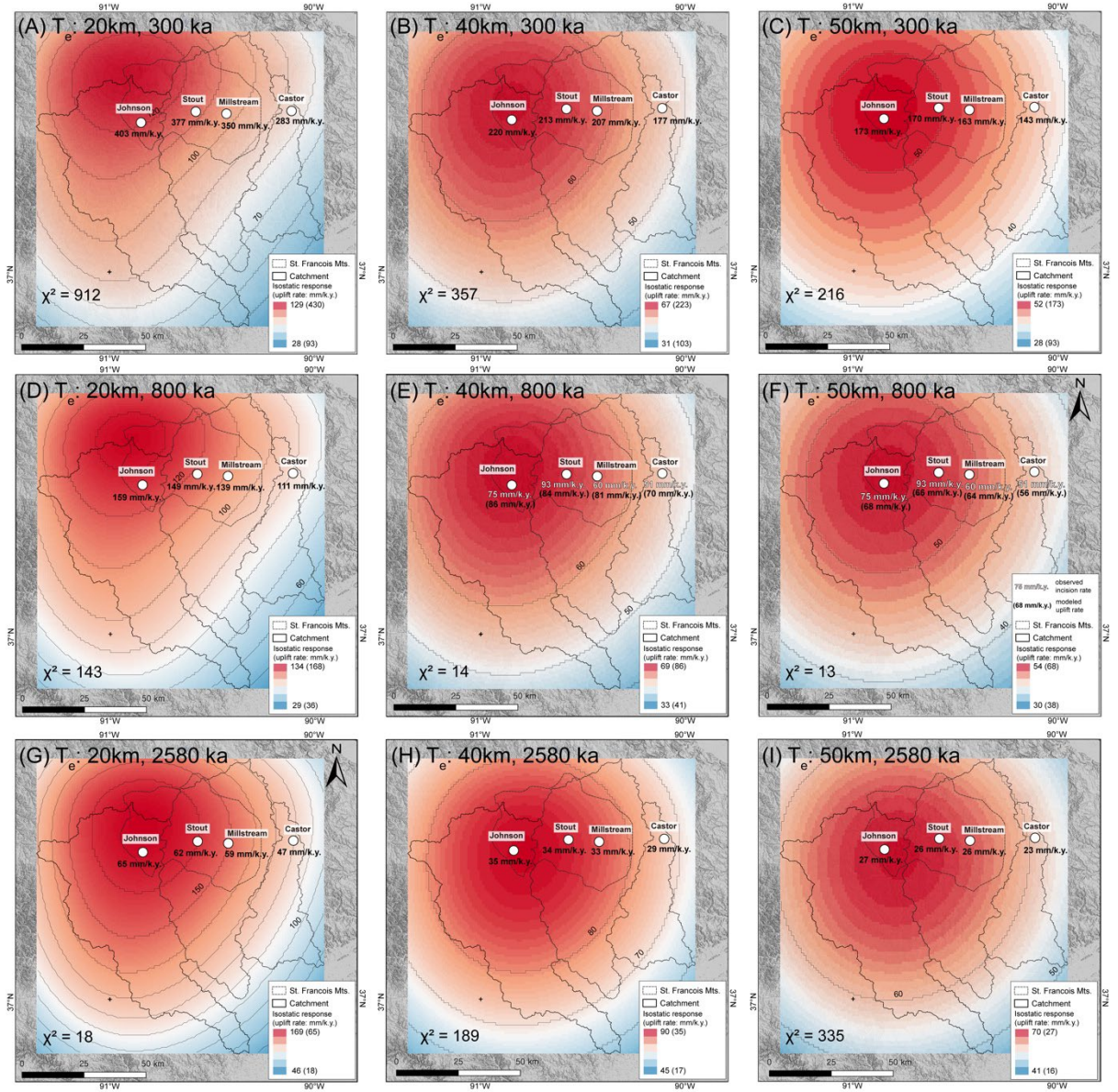


Figure S11. Complete set of nine isostatic-flexural models for three reasonable effective elastic thicknesses (increasing to the right) and geomorphic durations (increasing downward). Note: because model erosion occurs only once and at initial step rather than progressively, model uplift decays through time for all models. More sophisticated modeling is required to capture more realistic steady-state erosion.

6. Applying the χ^2 goodness of fit statistic to test observation (incision rates) – model (uplift rates) matches and misfits

χ^2 is a simple statistic used to measure goodness of fit, or in other words, observation-model misfits. In general terms, lower χ^2 values indicate better fits.

$$\chi^2 = \sum [(observed\ value_i - model\ value_i)/\sigma_i]^2 \quad (4)$$

The χ^2 statistic given in equation (4) is *not* the same as the χ topographic parameter (Perron & Royden, 2013; Scherler et al., 2017) discussed above.

Supplementary References:

Aydin, A., and Basu, A., 2005, The Schmidt hammer in rock material characterization: Engineering Geology, v. 81, no.1, p. 1-14.

Balco, G., Stone, J.O., Lifton, N.A., and Dunai, T.J., 2008, A complete and easily accessible means of calculating surface exposure ages or erosion rates from ^{10}Be and ^{26}Al measurements: Quaternary Geochronology, v. 3, p. 174–195.

Bechtel, T.D., Forsyth, D.W., Sharpton, V.L., and Grieve, R.A., 1990, Variations in effective elastic thickness of the North American lithosphere: Nature, 343(6259), 636-638.

Beeson, H.W., McCoy, S.W., and Keen-Zebert, A., 2017, Geometric disequilibrium of river basins produces long-lived transient landscapes: Earth and Planetary Science Letters, v. 475, p. 34-43.

Braucher, R., Del Castillo, P., Siame, L., Hidy, A.J., and Bourles, D.L., 2009, Determination of both exposure time and denudation rate from an in situ-produced ^{10}Be depth profile: a mathematical proof of uniqueness. Model sensitivity and applications to natural cases: Quaternary Geochronology, 4(1), 56-67.

Champagnac, J.D., Molnar, P., Anderson, R.S., Sue, C., and Delacou, B., 2007, Quaternary erosion-induced isostatic rebound in the western Alps: Geology, 35(3), 195-198.

Chmeleff, J., von Blanckenburg, F., Kossert, K., and Jakob, D., 2010, Determination of the ^{10}Be half-life by multicollector ICP-MS and liquid scintillation counting. Nuclear Instruments and Methods in Physics Research Section B: Beam Interactions with Materials and Atoms, 268(2), 192-199.

Creameens, D.L., Darmody, R.G., and George, S.E., 2005, Upper slope landforms and age of bedrock exposures in the St. Francois Mountains, Missouri: A comparison to relict periglacial features in the Appalachian Plateau of West Virginia: Geomorphology, v. 70, p. 71-84.

- Howard, A.D., Dietrich, W.E., and Siedl, M.A., 1994, Modeling fluvial erosion on regional to continental scales: *Journal of Geophysical Research*, v. 99, B7, p. 13971–13986, <https://doi.org/10.1029/94JB00744>.
- Hutton, E., Syvitski, J., 2008, Sedflux 2.0: An advanced process-response model that generates three-dimensional stratigraphy: *Computers & Geosciences*. 34(10), 1319-1337. <https://dx.doi.org/10.1016/j.cageo.2008.02.013>.
- Elez, J., Silva, P.G., and Martínez-Graña, A.M., 2020, Quantification of Erosion and Uplift in a Rising Orogen—A Large-Scale Perspective (Late Tortonian to Present): The Case of the Gibraltar Arc, Betic Cordillera, Southern Spain: *Remote Sensing*, 12(21), 3492.
- Kirby, E. and Ouimet, W.B., 2011, Tectonic geomorphology along the eastern margin of Tibet: insights into the pattern and processes of active deformation adjacent to the Sichuan Basin: *Geological Society, London, Special Publications*, v. 353, no. 1, p.165–188, doi:10.1144/SP353.9.
- Kohl, C.P., and Nishiizumi, K., 1992, Chemical isolation of quartz for measurement of in-situ-produced cosmogenic nuclides: *Geochimica et Cosmochimica Acta*, 56(9), 3583-3587.
- Korschinek, G., Bergmaier, A., Faestermann, T., Gerstmann, U. C., Knie, K., Rugel, G., ... & Remmert, A., 2010, A new value for the half-life of ^{10}Be by heavy-ion elastic recoil detection and liquid scintillation counting. *Nuclear Instruments and Methods in Physics Research Section B: Beam Interactions with Materials and Atoms*, 268(2), 187-191.
- Lal, D., 1991, Cosmic ray labeling of erosion surfaces: in situ nuclide production rates and erosion models: *Earth and Planetary Science Letters*, v. 104, p. 424–439.
- Lambeck, K., *The Slow Deformations of the Earth*, Clarendon Press, Oxford, UK, 718 pp., 1988.
- McKenzie, D. and Fairhead, D., 1997, Estimates of the effective elastic thickness of the continental lithosphere from Bouguer and free air gravity anomalies: *Journal of Geophysical Research: Solid Earth*, 102(B12), 27523-27552.
- Mudd, S.M., Harel, M.-A., Hurst, M.D., Grieve, S.W.D., and Marrero, S.M., 2016, The CAIRN method: automated, reproducible calculation of catchment-averaged denudation rates from cosmogenic nuclide concentrations: *Earth Surface Dynamics*, v. 4, p. 655-674.
- Murphy, B.P., Johnson J.P.L., Gasparini, N.M., and Sklar L.S., 2016, Chemical weathering as a mechanism for the climatic control of bedrock river incision: *Nature*, v. 532, p. 223-227.

- Nishiizumi, K., Imamura, M., Caffee, M.W., 2007, Absolute calibration of ^{10}Be AMS standards: Beam Interactions with Materials & Atoms, v. 258. p. 403-413, doi: 10.1016/j.nimb.2007.01.297
- Ouimet, W.B., Whipple, K.X., and Granger, D.E., 2009, Beyond threshold hillslopes: Channel adjustment to base-level fall in tectonically active mountain ranges: *Geology*, v. 37, no. 7, p. 579–582, doi: 10.1130/G30013A.1.
- Perron, J.T. and Royden, L., 2013, An integral approach to bedrock river profile analysis: *Earth Surface Processes and Landforms*, v. 38, p.570–576, doi: 10.1002/esp.3302.
- Scherler, D., Dibiase, R.A., Fisher, G.B., and Avouac, J.-P., 2017, Testing monsoonal controls 563 on bedrock river incision in the Himalaya and Eastern Tibet with a stochastic-threshold 564 stream power model: *Journal of Geophysical Research: Earth Surface*, v. 122, p. 1389–565 1429, doi:10.1002/2016JF004011.
- Schwanghart, W. and Scherler, D., 2014, Short Communication: TopoToolbox 2 – MATLAB569 based software for topographic analysis and modeling in Earth surface sciences: *Earth Surface Dynamics*, v. 2, p.1–7, doi:10.5194/esurf-2-1-2014.
- Snyder, N.P., Whipple, K.X., Tucker, G.E., and Merritts, D.J., 2000, Landscape response to tectonic forcing: Digital elevation model analysis of stream profiles in the Mendocino triple junction region, northern California: *Geological Society of America Bulletin*, 112(8), 1250-1263.
- Stone, J.O., 2000, Air pressure and cosmogenic isotope production: *Journal of Geological Society of London*, v. 105, no. B10, p.753–759.
- Viles, H., Goudie, A., Grab, S., and Lalley, J., 2011, The use of the Schmidt Hammer and Equotip for rock hardness assessment in geomorphology and heritage science: a comparative analysis: *Earth surface processes and landforms*, 36(3), 320-333.
- Watts, A.B., 2001, *Isostasy and Flexure of the Lithosphere*: Cambridge, UK, Cambridge University Press, 458 p.
- Williams, R.B.G., and Robinson, D.A., 1983, The effect of surface texture on the determination of the surface hardness of rock using the Schmidt hammer: *Earth Surface Processes and Landforms*, 8(3), 289-292.
- Wobus, C., Whipple, K.X., Kirby, E., Snyder, N., Johnson, J., Spyropolou, K., Crosby, B., and Sheehan, D., 2006, Tectonics from topography: Procedures, promise, and pitfalls, in Willett, S.D., et al., eds., *Tectonics, Climate, and Landscape Evolution*: Geological Society of America Special Papers, v. 398, p. 55–74, [https://doi.org/10.1130/2006.2398\(04\)](https://doi.org/10.1130/2006.2398(04)).

Zhang, H., Zhang, P., Champagnac, J. D., Molnar, P., Anderson, R. S., Kirby, E., Craddock, W., and Liu, S., 2014, Pleistocene drainage reorganization driven by the isostatic response to deep incision into the northeastern Tibetan Plateau: *Geology*, 42(4), 303-306.